THE JOURNAL OF BIOLOGICAL CHEMISTRY Vol. 280, No. 15, Issue of April 15, pp. 15071–15083, 2005
Printed in U.S.A.

Mechanism of Action of Myosin X, a Membrane-associated Molecular Motor*

Received for publication, January 18, 2005, and in revised form, February 9, 2005
Published, JBC Papers in Press, February 10, 2005, DOI 10.1074/jbc.M500616200

Mihály Kovács‡, Fei Wang, and James R. Sellers

From the Laboratory of Molecular Physiology, NHLBI, National Institutes of Health, Bethesda, Maryland 20892-1762

We have performed a detailed biochemical kinetic and spectroscopic study on a recombinant myosin X head construct to establish a quantitative model of the enzymatic mechanism of this membrane-bound myosin. Our model shows that during steady-state ATP hydrolysis, myosin X exhibits a duty ratio (*i.e.* the fraction of the cycle time spent strongly bound to actin) of around 16%, but most of the remaining myosin heads are also actin-attached even at moderate actin concentrations in the so-called "weak" actin-binding states. Contrary to the high duty ratio motors myosin V and VI, the ADP release rate constant from actomyosin X is around five times greater than the maximal steady-state ATPase activity, and the kinetic partitioning between different weak actin-binding states is a major contributor to the rate limitation of the enzymatic cycle. Two different ADP states of myosin X are populated in the absence of actin, one of which shows very similar kinetic properties to actomyosin·ADP. The nucleotide-free complex of myosin X with actin shows unique spectral and biochemical characteristics, indicating a special mode of actomyosin interaction.

Myosin X is a recently described member of the myosin superfamily that is expressed in vertebrate tissues as a single isoform (1, 2). The heavy chain of myosin X consists of an N-terminal motor domain containing the actin- and ATP-binding sites, a neck region that binds three calmodulin (or possibly other) light chains, a putative coiled-coil region that may bring about heavy chain dimerization, and a tail region consisting of several domains of effector function (three pleckstrin homology (PH3)[1] domains, a MyTH4, and a FERM domain) (1). The presence of the PH3 domains in the myosin X tail is a unique feature among myosins, and it enables this myosin to directly bind to the plasma membrane via phosphatidylinositol phospholipids (1, 3). Myosin X has been shown to localize to regions of dynamic actin and to exhibit remarkable patterns of intrafilopodial motility (1, 4). Most interestingly, myosin X localizes to the tips of filopodia, which appears to be an active process requiring myosin X motor function (4). Myosin X induces elongation of filopodia by transporting the Mena-VASP complex (an inhibitor of actin filament capping) to filopodial tips (5). Myosin X activity is also necessary for phagocytosis (6) as well as the localization and function of integrins (7).

The above functional studies indicate a cellular role for myosin X as a plasma membrane-associated cargo transporter. This setting is unique within the myosin superfamily, which implies that this class of motors may have adapted to its role by acquiring distinctive molecular properties. All myosins exert their motile activity during a cyclic interaction with actin filaments and ATP. The enzymatic parameters are key determinants of the motile output of motor proteins, and it has been shown in numerous cases that the biochemistry of different myosins reflects precise and profound functional adaptations to their widely differing cellular roles (for a review see Ref. 8). Studies on a heavy meromyosin-like recombinant fragment of myosin X have shown that myosin X exhibits actin-activated ATPase activity and *in vitro* motility directed toward the barbed end of actin filaments (9). Its mechanism of action, however, has not been investigated in detail. To assess the biochemical and enzymatic properties of myosin X, we used the baculovirus-Sf9 expression system to produce a single-headed myosin X construct (named mX-S1) that retains the catalytically active portion of the molecule. We performed steady-state and transient kinetic, fluorescence spectroscopic, and other biochemical measurements to show that myosin X spends a relatively small fraction (16%) of its ATPase cycle time in the so-called strong actin-binding states. This behavior suggests that myosin X does not use a myosin V-like single molecule processive stepping mechanism. However, the total actin attachment ratio of myosin X during steady-state ATP hydrolysis is notably high even at moderate actin concentrations (>50% attachment at 20 μM actin). This feature is due to the kinetic partitioning between different "weak" actin-binding states, which may greatly aid in maintaining continuous actin attachment and therefore proper functioning of a small array of membrane-bound motors.

EXPERIMENTAL PROCEDURES

Cloning, Expression, and Purification of mX-S1—A truncated (subfragment-1-like) fragment of the bovine myosin X heavy chain cDNA (gift of Dr. David Corey, Harvard Medical School) encoding the motor domain and all three light chain-binding motifs (first 810 amino acids of the heavy chain) was cloned into the pVL1392 expression vector. This construct (referred to as mX-S1 throughout this paper) was coexpressed with calmodulin in the baculovirus-Sf9-expression system. A C-terminal FLAG tag (sequence DYKDDDDK) was appended to the heavy chain that enabled high purity (>99%) preparation of recombinant mX-S1. Expression and purification procedures were as described earlier for non-muscle myosin IIA heavy meromyosin (10). Typically, 2–5 mg of mX-S1 could be purified from 4×10^9 Sf9 cells. Purified mX-S1 was stored in a high ionic strength (I = 525 mM) buffer and used within 4 days of preparation or flash-frozen immediately. The construct was not soluble at low ionic strengths in the absence of actin and nucleotide. Therefore, ionic strengths of >30 mM had to be used in most experiments. A 2-fold molar excess of extra calmodulin was added to mX-S1

* The costs of publication of this article were defrayed in part by the payment of page charges. This article must therefore be hereby marked "*advertisement*" in accordance with 18 U.S.C. Section 1734 solely to indicate this fact.

‡ To whom correspondence should be addressed: Laboratory of Molecular Physiology, NHLBI, National Institutes of Health, Bethesda, MD 20892-1762. Tel.: 301-496-6887; Fax: 301-402-1542; E-mail: kovacsm@mail.nih.gov.

[1] The abbreviations used are: PH3, pleckstrin homology domain 3; mant, methylanthraniloyl-; MDCC-PBP, fluorescently labeled bacterial phosphate-binding protein; MOPS, *N*-morpholinopropanesulfonic acid; mX-S1, recombinant subfragment-1 like bovine myosin X construct; S1, subfragment-1; ATPγS, adenosine 5′-*O*-(thiotriphosphate).

after purification in order to fully saturate the binding sites on the mX-S1 heavy chain, thereby preventing protein aggregation. Protein concentrations were determined using the Bio-Rad assay using smooth muscle myosin subfragment-1 as a standard. Stopped-flow-based active site titrations with mant-ATP indicated that the error of protein concentration determinations was below 10%.

Other Materials—Rabbit skeletal muscle myosin and subfragment-1 (S1) were prepared as described in Refs. 11 and 12, respectively. Recombinant non-muscle myosin IIB S1 was prepared as described earlier for non-muscle myosin IIA heavy meromyosin (10). Actin was prepared as described in Ref. 13 and pyrene labeled as described in Ref. 14. Actin filaments were stabilized by addition of a 1.5-fold molar excess of phalloidin (Calbiochem) in all experiments. Mant-ATP and pyrene-iodoacetamide were purchased from Molecular Probes. MDCC-PBP (fluorescently labeled bacterial P_i-binding protein) (15) was generously provided by Dr. Howard D. White (Eastern Virginia Medical School). Other reagents were from Sigma.

Fluorescence Spectroscopy—Pyrene fluorescence excitation and emission spectra were recorded using a SPEX FluoroMax-3 spectrofluorometer at 25 °C in a buffer comprising 20 mM MOPS (pH 7.0), 5 mM $MgCl_2$, 100 mM KCl, and 0.1 mM EGTA (I = 125 mM). In acrylamide quenching, steady-state fluorescence anisotropy, and temperature dependence measurements, samples containing pyrene-actin were excited at 347 nm (1 nm bandwidth), and emission was monitored at 406 nm (5 nm bandwidth). Background signal measured with assay buffer alone was subtracted from all fluorescence records before analysis.

Acto-S1 Cosedimentation—Samples were set up at room temperature under the same buffer conditions as in the spectroscopic measurements (or using 20 mM instead of 100 mM KCl to yield a final I = 45 mM where indicated) and then ultracentrifuged at 100,000 rpm in a Beckman TLA-100 rotor for 15 min at 4 °C, and the supernatants and pellets were run on 4–20% SDS-polyacrylamide gels. In samples involving ATP but not ADP, contaminating amounts of ADP were removed by the addition of 200 units/ml pyruvate kinase and 1 mM phosphoenolpyruvate. Protein amounts in electrophoretic bands were quantified by densitometric analysis using the Kodak ID 3.5 software.

Steady-state Kinetics—Steady-state MgATPase activities were measured by a NADH-linked assay as described earlier (16, 17) in a buffer containing 4 mM MOPS (pH 7.0), 2 mM $MgCl_2$, 0.1 mM EGTA, 1 mM ATP, 40 units/ml lactate dehydrogenase, 200 units/ml pyruvate kinase, 1 mM phosphoenolpyruvate, 0.2 mM NADH plus various concentrations of KCl (I = 10 mM + [KCl]). Data were corrected for background ATPase activity of actin.

Transient Kinetics—Stopped-flow experiments were performed in a KinTek SF-2001 apparatus. Tryptophan fluorescence was excited at 295 nm (6 nm bandwidth), and emission was selected using a 347-nm band-pass filter with a 50 nm bandwidth. Pyrene fluorescence was excited at 365 nm (6 nm bandwidth), and emission monitored through a 400 nm long-pass filter. Light scattering was measured at 420 nm in samples containing pyrene-actin. Mant-ATP was excited using energy transfer from nearby tryptophan residues (excitation at 280 nm with 6 nm bandwidth; emission, 400 nm long-pass filter). MDCC-PBP fluorescence was excited at 436 nm (6 nm bandwidth), and emission was collected through a 450 nm long-pass filter. Quenched-flow experiments were performed in a KinTek RQF-3 apparatus using [γ-^{32}P]ATP as described earlier (17).

Post-mixing concentrations are indicated throughout the text unless stated otherwise. The volume ratio was 1:1 in all single mixing, and 5:2:5 in double-mixing experiments. Nucleotide-free mX-S1 and acto-mX-S1 were prepared by incubation with 0.01 units/ml apyrase for 15 min at room temperature. In phosphate release measurements, all solutions were preincubated with a "P_i mop" consisting of 0.02 units/ml purine nucleoside phosphorylase and 0.5 mM 7-methylguanosine.

Data Analysis and Kinetic Modeling—Reported means and S.D. are those of two to six rounds of experiment. Fitting of the data sets to mathematical functions was done using the KinTek SF-2001 software and OriginLab 7.0 (Microcal Corp.). Kinetic simulations and global fitting analyses were performed using the Gepasi version 3.21 software (Pedro Mendes, Virginia Bioinformatics Institute).

RESULTS

Basal ATPase Mechanism of mX-S1—In all experiments of the present study, we used a single-headed myosin X construct (mX-S1) that contains the catalytically active motor domain as well as the entire neck region comprising three light chain-binding IQ motifs and three calmodulin molecules as light chains.

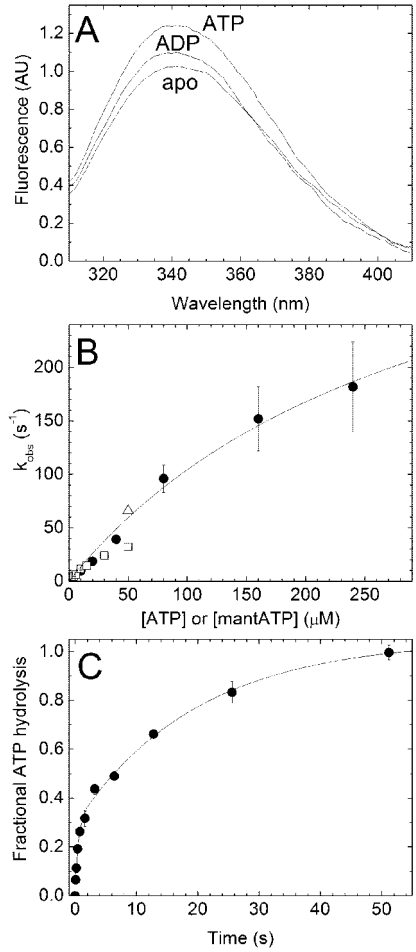

FIG. 1. **ATP binding and hydrolysis by mX-S1 in the absence of actin.** *A*, tryptophan fluorescence emission spectra of 5 μM mX-S1 in the absence of nucleotide (*apo*) and after the addition of 300 μM ADP or 300 μM ATP. Fluorescence was excited at 295 nm with 1 nm bandwidth, and emission was detected using a bandwidth of 5 nm. *B*, observed rate constants (k_{obs}) of single exponential fits to tryptophan fluorescence transients recorded on mixing 0.5 μM mX-S1 with different concentrations of ATP in the stopped-flow apparatus (*solid circles*). A hyperbolic fit of the dependence of k_{obs} on [ATP] yielded a maximal k_{obs} of 430 ± 80 s^{-1} with half-saturation at 310 ± 90 μM ATP. The *open triangle* shows the k_{obs} of the exponential burst phase of P_i production in a quenched-flow experiment, where 1.7 μM mX-S1 was mixed with 50 μM ATP (k_{obs} = 67 ± 15 s^{-1}, see text). The *open squares* indicate the k_{obs} values of the single exponential increase in mant-ATP fluorescence on mixing 0.5 μM mX-S1 with various mant-ATP concentrations in the stopped flow. *C*, time course of ATP hydrolysis upon mixing 2.3 μM mX-S1 with 1 μM [γ-^{32}P]ATP in the quenched-flow apparatus (single turnover conditions). A double exponential approximation to the reaction time profile indicated a burst phase (k_{obs} = 2.1 s^{-1}) with a fractional amplitude (= $A_{fast}/(A_{fast} + A_{slow})$) of 0.28, whereas the slow phase of the reaction had a k_{obs} of 0.03 s^{-1}. Conditions are as follows: 25 °C, 20 mM MOPS (pH 7.0), 5 mM $MgCl_2$, 100 mM KCl and 0.1 mM EGTA. *Error bars* indicate S.D. for n = 3.

The tryptophan fluorescence emission of mX-S1 showed a 6% increase and a small (3 nm) blue shift on the addition of ADP (Fig. 1*A*). The addition of ATP to mX-S1 caused a similar blue shift and a 20% fluorescence enhancement compared with the nucleotide-free state, indicating that at least one intermediate of higher fluorescence than the mX-S1·ADP complex is significantly populated during steady-state ATP hydrolysis (Fig. 1*A*). Mixing mX-S1 with ATP under pseudo first-order conditions in the stopped-flow apparatus yielded single exponential tryptophan fluorescence transients (traces not shown). The dependence of the fitted observed rate constants (k_{obs}) of these traces on ATP concentration showed signs of saturation above 250 s^{-1} as shown in Fig. 1*B*. This behavior suggests that ATP binding

$$\overset{\qquad\qquad\qquad\qquad\qquad\qquad K_D}{\overbrace{\qquad\qquad\qquad\qquad\qquad\qquad}}$$

$$\overset{K_1}{\mathrm{M}} \leftrightarrow \overset{k_2}{\mathrm{MT}} \rightarrow \overset{K_3}{\mathrm{M^*T}} \leftrightarrow \overset{k_4}{\mathrm{M^{**}DP}} \rightarrow \overset{K_5}{\mathrm{M^*D}} \leftrightarrow \overset{K_6}{\mathrm{MD}} \leftrightarrow \mathrm{M}$$

SCHEME 1. **Equilibrium constants are expressed as dissociation constants or for first-order transitions in a left-to-right direction in all schemes.** *Arrows* for associating or dissociating components are omitted for clarity in all schemes except Scheme 4. *Asterisks* indicate states with elevated tryptophan fluorescence. Abbreviations used are as follows: *A*, actin; *M*, myosin; *T*, ATP; *D*, ADP; *P*, phosphate.

to mX-S1 is a two-step process (K_1 and k_2 in Scheme 1), and the maximal k_{obs} value largely reflects a first-order isomerization step during the binding process (k_2). The ATP hydrolysis step ($k_3 + k_{-3}$) is associated with a further increase in tryptophan fluorescence (*cf.* Scheme 1), and it may therefore have contributions to the ATP-binding k_{obs} values of Fig. 1*B*. The quasi-linear part of the plot at low [ATP] indicated an apparent second-order ATP-binding rate constant (k_2/K_1) of 1.1 μM^{-1} s^{-1} (Fig. 1*B* and Table I). k_{obs} values for ATP binding obtained by monitoring the signal of mant-ATP, a fluorescently labeled substrate, showed a very similar profile to the tryptophan results (Fig. 1*B* and Table I).

The time course of transient state ATP hydrolysis by mX-S1 was followed using the quenched-flow technique. In a single turnover experiment shown in Fig. 1*C*, cleavage of ATP followed a biphasic time profile with the fast burst phase being rate-limited by ATP binding and the slow phase by product release that is slower than the ATP cleavage step. The equilibrium constant of ATP hydrolysis in the enzyme-bound state (K_3) was 0.3 ± 0.1, as calculated from the amplitude data ($K_3 = A_{fast}/A_{slow}$). The results of multiple turnover quenched-flow experiments in which 1 μM mX-S1 was mixed with a large excess of ATP (50 μM) confirmed the above K_3 value and gave a k_{obs} of the burst of 67 ± 15 s^{-1}, indicating that ATP binding is still rate-limiting at this ATP concentration (*i.e.* the ATP hydrolysis rate constant ($k_3 + k_{-3}$) is greater than this k_{obs} value, traces not shown; see Fig. 1*B* and Table I).

Phosphate release from the mX-S1·ADP·P_i complex was monitored using a fluorescently labeled P_i-binding protein (MDCC-PBP). The time course of P_i release on mixing 1 μM mX-S1 with 0.6 μM ATP (single turnover conditions) was a single exponential with a k_{obs} of 0.03 s^{-1}, a value identical to the steady-state ATPase activity of mX-S1 in the absence of actin, as measured by an NADH-linked coupled assay (traces not shown; Table I). This indicates that the P_i release is rate-limiting in the basal (*i.e.* in the absence of actin) ATPase cycle of mX-S1, with its k_{obs} being determined by the kinetic partitioning in the hydrolysis step (K_3) and the fundamental P_i release rate constant (k_4) as $k_{obs,P_i} = k_4K_3/(1 + K_3)$ (Scheme 1 and Table I).

Although most of the above features of the basal mX-S1 ATPase cycle are similar to those of other myosins, the ADP interaction of mX-S1 showed some remarkably unusual properties. On mixing mX-S1 with ADP in the stopped-flow under pseudo first-order conditions, the single exponential k_{obs} values of the recorded tryptophan fluorescence transients slightly increased with increasing [ADP] and saturated around the low value of 4 s^{-1} (Fig. 2*A*). At first glance, the data could seem to indicate a low affinity single step binding mechanism with a relatively high intercept ($k_{off} \approx 2$ s^{-1}) and a small linear slope ($k_{on} < 0.1$ μM^{-1} s^{-1}). However, the ADP binding affinity should then be low ($K_d = k_{off}/k_{on} > 20$ μM), which is ruled out by the fact that the amplitudes of the transients showed saturation at much lower ADP concentrations (K_d = 1.0 ± 0.2 μM, Fig. 2*A*, *inset*). Another possible explanation for the obtained k_{obs} values comes from a two-step model (*cf.* the *right* part of Scheme 1 comprising K_5 and K_6, viewed right to left in the direction of ADP binding). In this model the ADP-binding process consists of an initial rapid equilibrium (K_6, no signal change on this step) followed by a slower reversible isomerization accompanied by a fluorescence increase (K_5). The intercept of Fig. 2*A* will thus be mostly determined by k_5 (≈1.5 s^{-1}, going left-to-right in Scheme 1); the maximal k_{obs} will indicate $k_5 + k_{-5}$ (≈4.5 s^{-1}), and half-saturation will occur at [ADP] = K_6 (≈5 μM). To test further the validity of this model, we performed ADP "chasing" stopped-flow experiments in which equilibrium mixtures of mX-S1 and ADP were rapidly mixed with mant-ATP in at least 5-fold excess over ADP to ensure that ADP dissociation after the rapid mix is essentially irreversible (Fig. 2*B*). The observed mant-ATP fluorescence transients were biphasic throughout the examined [ADP] range (Fig. 2*B, inset*). The fractional amplitude of the slow phase ($A_{slow}/(A_{fast} + A_{slow})$) was saturated at 0.73 ± 0.02 and reached half-maximum at 1.7 ± 0.2 μM ADP. These data are consistent with the above two-step mechanism inasmuch as the fractional amplitude of the fast phase is determined by the combined fractional population of the M and MD species (*cf.* Scheme 1) that allows fast binding of mant-ATP, whereas the slow phase comes from M*D first slowly isomerizing to MD, then losing ADP, and binding mant-ATP. At high [ADP], the A_{fast}/A_{slow} ratio will then equal [MD]/[M*D] (because[M] = 0 in the preincubation mixture) and thus K_5 = 0.37 ± 0.03. Furthermore, at high [ADP], k_{fast} and k_{slow} will equal k_6 (= 15 s^{-1}, left-to-right in Scheme 1, *cf.* Fig. 2*B, inset*) and k_5 (= 1.3 s^{-1}), respectively. From the experimental data shown in Fig. 2, *A* and *B*, all rate and equilibrium constants of the two-step ADP-binding process can be calculated as shown in Table I.

Fig. 2*C* shows experiments that provide a further confirmation of the above model. Here 0.7 μM mX-S1 was mixed in the stopped flow with a nucleotide mixture consisting of 50 μM ATP and various ADP concentrations. The resulting tryptophan fluorescence transients were fitted to single exponentials (Fig. 2*C*, *inset*). It is noteworthy that when the two nucleotides were in equimolar amounts, the k_{obs} of the trace (12 s^{-1}, *trace 2* in Fig. 2*C, inset*) was only 17% that in the absence of ADP (70 s^{-1}, *trace 1*). This behavior rules out a slow, single step binding of ADP with a k_{obs} around 4 s^{-1} (*cf.* Fig. 2*A*). The *open symbols* in Fig. 2*C* show the k_{obs} values of single exponential fits to simulated fluorescence transients based on a model of competitive binding of ATP (k_2/K_1 = 1.4 μM^{-1} s^{-1}) and ADP (k_5 = 1.1 s^{-1}, k_{-5} = 3.1 s^{-1}, k_6 = 15 s^{-1}, k_{-6} = 3 μM^{-1} s^{-1}, *cf.* Scheme 1, rate constants estimated from the above experimental results) to mX-S1 where the tryptophan fluorescence enhancement assigned to ATP binding was twice that of the MD ↔ M*D

TABLE I
Kinetic parameters of the basal ATPase cycle of mX-S1

The conditions used are as follows: 25 °C, 20 mM MOPS (pH 7.0), 5 mM $MgCl_2$, 100 mM KCl, 0.1 mM EGTA. Means ± S.D. for n = 3 are reported. Numbering of steps refers to Scheme 1.

k_2/K_1 (μM^{-1} s^{-1}) (mant-ATP)	1.1 ± 0.1
k_2/K_1 ($\mu M^{-1}s^{-1}$) (tryptophan)	1.1 ± 0.1
k_2 (s^{-1}) (tryptophan)	>250
K_3 (quenched flow)	0.3 ± 0.1
$k_3 + k_{-3}$ (s^{-1}) (quenched flow, tryptophan)	>80
$k_{obs,Pi}$ (s^{-1}) (quenched flow, MDCC-PBP)	0.03 ± 0.01
k_4 (s^{-1}) (calculated as $k_{obs,Pi}(1 + K_3)/K_3$)	0.13
K_5 (ADP chasing with mant-ATP)	0.37 ± 0.03
k_5 (s^{-1}) (tryptophan, ADP chasing with mant-ATP)	1.1–1.3
k_{-5} (s^{-1}) (tryptophan, ADP chasing with mant-ATP)	3.1
K_6 (μM) (calculated as $K_D(1 + K_5)/K_5$)	3.7–6.3
k_6 (s^{-1}) (tryptophan, ADP chasing with mant-ATP)	13–16
k_{-6} (μM^{-1} s^{-1}) (calculated as k_6/K_6)	2.1–4.3
K_D (μM) (ADP chasing with mant-ATP, amplitudes)	1.7 ± 0.2
K_D (μM) (tryptophan, amplitudes)	1.0 ± 0.2
Steady-state ATPase k_{cat} (s^{-1}) (NADH-linked assay)	0.03 ± 0.01

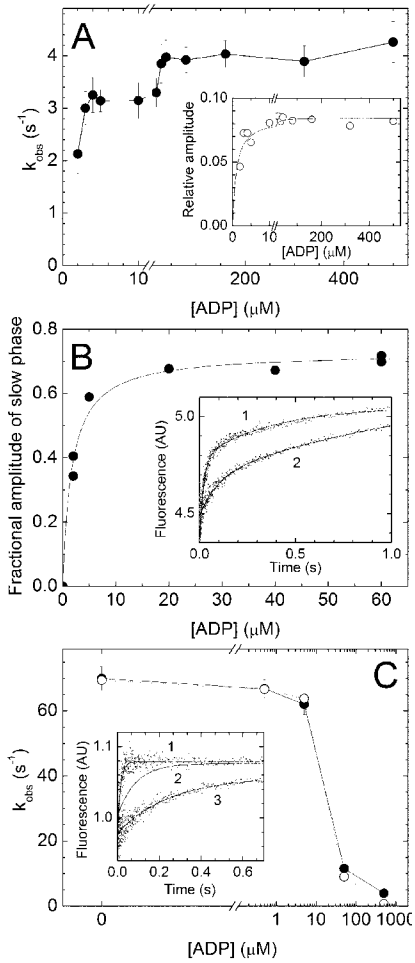

FIG. 2. **ADP interaction of mX-S1 in the absence of actin.** *A*, observed rate constants (k_{obs}) of single exponential fits to tryptophan fluorescence transients obtained on mixing 0.4 μM mX-S1 with different concentrations of ADP in the stopped-flow. The *inset* shows relative amplitudes of the same reactions (fluorescence level before mix was taken as unity). A hyperbolic fit to the amplitude data yielded a maximal relative amplitude of 0.085 ± 0.002 with half-saturation at 1.0 ± 0.2 μM ADP. Note the breaks in the *x* axes of both panels. *B*, fractional amplitude of the slow phase (= $A_{slow}/(A_{fast} + A_{slow})$)of the double exponential mant-ATP fluorescence transients on rapid mixing of 0.5 μM mX-S1 plus the indicated ADP concentrations with mant-ATP (in at least 5-fold molar excess over ADP) in the stopped flow. The data were fitted to a hyperbola to yield a maximal fractional amplitude of 0.73 ± 0.02 for the slow phase with half-saturation at 1.7 ± 0.2 μM ADP. The *inset* shows traces for two of the data points. *Trace 1* was obtained on mixing 0.5 μM mX-S1 and 2 μM ADP with 50 μM mant-ATP (k_{fast} = 48 s^{-1} (59% amplitude); k_{slow} = 2.8 s^{-1} (41%)). In *trace 2*, 0.5 μM mX-S1 and 60 μM ADP was mixed with 300 μM mant-ATP (k_{fast} = 13 s^{-1} (29% amplitude); k_{slow} = 1.3 s^{-1} (71%)). Pre-mixing concentrations are indicated in this panel. *C*, observed rate constants (k_{obs}) of single exponential fits to tryptophan fluorescence transients recorded on rapidly mixing 0.7 μM mX-S1 with a pre-mixture of 50 μM ATP plus ADP at the indicated concentrations (*solid symbols*). The *open symbols* indicate the fitted rate constants of simulated time courses obtained using the kinetic model described in the text. *Traces 1–3* of the *inset* are experimental tryptophan fluorescence transients of the data points at 0, 50, and 500 μM ADP, respectively (fitted rate constants are 70, 12, and 3.9 s^{-1}). Conditions were as in Fig. 1. *Error bars* indicate fitting errors of k_{obs}.

transition (no fluorescence change occurs on step 6). The simulated transients were clearly double exponential in most cases, but single exponential approximations were applied because the experimental signal-to-noise ratio did not allow the resolution of multiple phases (*cf.* Fig. 2*C, inset*). This approximation was fully suitable for the discrimination of the two ADP-binding models discussed above.

TABLE II
Actin-activated steady-state ATPase parameters of mX-S1

The conditions used are as follows: 25 °C, 2 mM MOPS (pH 7.0), 2 mM $MgCl_2$, 0.1 mM EGTA, 1 mM ATP plus KCl to yield the stated ionic strengths. Means ± S.D. for n = 3 are reported.

I	V_{max}	K_{ATPase}
mM	s^{-1}	μM
10	4.0 ± 1.5	5.1 ± 0.6
30	5.3 ± 0.3	7.3 ± 1.0
60	5.3 ± 2.1	36 ± 8
110	3.0 ± 1.0	33 ± 5

A chasing experiment in which the pre-mixture of 0.7 μM mX-S1 and 50 μM ADP was rapidly mixed with 500 μM ATP gave a tryptophan fluorescence increase transient with a fitted single exponential k_{obs} of around 16 s^{-1} (trace not shown). This value is remarkably higher than the intercept of the ADP-binding transients in Fig. 2*A*. This behavior is consistent with the two-step model described in the previous paragraph, which predicts this experiment to yield a transient consisting of a major phase dominated by k_6 (≈15 s^{-1}) and a slower phase (k_5 ≈1.2 s^{-1}) with a small amplitude (the two phases did not appear separate because of the low experimental signal-to-noise ratio).

Actin Activation of the Steady-state ATPase Activity—The steady-state ATPase activity of mX-S1 was ~100-fold activated by actin to a V_{max} around 4 s^{-1} as measured by an NADH-linked coupled enzyme assay (Table II and Fig. 3). Although the V_{max} value was fairly independent of solution ionic strength, the actin concentration needed for half-maximal activation (K_{ATPase}) markedly increased with increasing ionic strength (Table II). This behavior is characteristic of myosins in which the so-called weak actin-binding (ATP or ADP·P_i-bound) myosin states are the predominant steady-state intermediates in the actomyosin ATPase cycle. The steady-state data are in line with those reported by Homma *et al.* (9) for a heavy meromyosin-like myosin X construct (V_{max} = 4.7 s^{-1}, K_{ATPase} = 28 μM at 25 °C, I = 40 mM in the absence of Ca^{2+}).

Strong Binding Interaction of mX-S1 with Actin—Actin site-specifically labeled with pyrene at residue Cys-374 has been widely used to probe the so-called strong actomyosin interaction (*i.e.* that in nucleotide-free actomyosin and in the actomyosin·ADP ternary complex) (18, 19). We used this system to monitor the actin interaction of mX-S1. Fig. 4*A* shows pyrene fluorescence excitation and emission spectra of free pyrene-actin, pyrene-acto-mX-S1, and pyrene-acto-myosin II S1. These spectra indicate that the large quench (>60% at 365 nm excitation) occurring on the binding of myosin II (and other myosins including myosins V and VI) to pyrene-actin results largely from the selective quench of the 360 and 365 nm excitation peaks, consistently with the original study of Kouyama and Mihashi (19). In contrast to this, the smaller (<30%) quench on mX-S1 binding to pyrene-actin is not accompanied by a significant change in the relative intensities of the excitation peaks (Fig. 4*A*). This feature suggests that the strong binding interaction of mX-S1 with actin is structurally different from that of the myosins mentioned above. Addition of 300 μM ATP or ATPγS (nucleotides that induce actomyosin dissociation) to pyrene-acto-mX-S1 fully reversed the fluorescence quench, whereas a partial reversal was observed on adding 300 μM ADP, likely because of partial dissociation of mX-S1 from actin (data not shown).

The small quench in pyrene-acto-mX-S1 is not a result of incomplete saturation of pyrene-actin with mX-S1, as evidenced by fluorescence titrations shown in Fig. 4*B*. Titration of pyrene-actin with mX-S1 in a spectrofluorometer yielded a small maximal quench (16%; the extent of the measured fluo-

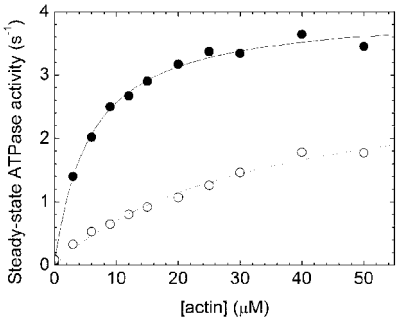

FIG. 3. **Actin activation of the mX-S1 ATPase.** Actin-activated steady-state ATPase activity of mX-S1 (50 nM) at ionic strengths of 10 mM (*solid symbols*) and 110 mM (*open symbols*). Hyperbolic fits to the data sets yielded a V_{max} of 4.0 ± 0.1 s^{-1} and a K_{ATPase} of 5.7 ± 0.4 μM (I = 10 mM), and a V_{max} of 3.0 ± 0.3 s^{-1} and a K_{ATPase} of 33 ± 5 μM (I = 110 mM). Conditions are as follows: 25 °C, 4 mM MOPS (pH 7.0), 2 mM $MgCl_2$, 0.1 mM EGTA, 1 mM ATP, 40 units/ml lactate dehydrogenase, 200 units/ml pyruvate kinase, 1 mM phosphoenolpyruvate, 0.2 mM NADH plus KCl to yield the stated ionic strengths. The basal ATPase activity of mX-S1 (0.03 s^{-1}) was subtracted from all data points.

rescence change was smaller than in Fig. 4*A* because of the different excitation/emission set up). At saturating mX-S1 concentrations, sequential additions of unlabeled acto-mX-S1 did not further lower the fluorescence of pyrene-acto-mX-S1, which rules out the possibility that the observed decrease in pyrene fluorescence is a light-scattering artifact (data not shown). Fig. 4*B, inset,* shows a stopped-flow-based amplitude titration where pyrene-acto-mX-S1 was rapidly mixed with excess ATP in order for all mX-S1s to depart from the strong binding acto-mX-S1 complex. The dissociation constant of mX-S1 binding to pyrene-actin calculated from the experiments in Fig. 4*B* (K_A = 0.14 ± 0.05 μM; *cf.* Scheme 2 and Table IV) was remarkably higher than that of other myosins studied (K_A usually falls between 10 pM and 10 nM) (17, 20–26).

Further fluorescence characterization also indicated a unique mode of interaction of mX-S1 with pyrene-actin in the absence of nucleotide. Acrylamide quenching measurements showed that the Stern-Volmer quenching constant of pyrene-actin reduced 5–10-fold on binding to different myosin II isoforms (Table III), reflecting a marked reduction in the solvent exposure of the pyrene fluorophore attached to Cys-374 of actin. The reduction was much smaller (2.5-fold) in the case of mX-S1 (Table III). Also, the steady-state fluorescence anisotropy of the pyrene-acto-mX-S1 complex showed an intermediate value between those of free pyrene-actin and pyrene-acto-myosin II S1, although the differences were small (Table III). The temperature dependence of pyrene-acto-mX-S1 fluorescence intensity (both in the absence of nucleotide and in the presence of 300 μM ADP) closely paralleled that of free pyrene-actin; it decreased by ~1% per 1 °C temperature increase between 5 and 25 °C, which is likely due solely to a physical effect and not to protein conformational changes (data not shown) (27). This result rules out the possibility that the limited effect of mX-S1 binding on pyrene-actin fluorescence (intensity, solvent exposure, and anisotropy) would come from temperature-sensitive conformational heterogeneity.

We investigated the kinetics of pyrene-actin binding to mX-S1 by mixing the two proteins under pseudo first-order conditions in the stopped flow (Fig. 4*C*). The dependence of k_{obs} values of single exponential fits to the pyrene fluorescence transients delineated an ~8-fold slower second-order binding rate constant in the presence of ADP (k_{-DA} = 0.26 ± 0.02 μM^{-1} s^{-1}) than in the absence of nucleotide (k_{-A} = 2.1 ± 0.2 μM^{-1} s^{-1}) (Table IV and Scheme 2). The off-rate constants (k_A and k_{DA}) determined by the intercepts of the plots were in the range of 0.4–1 s^{-1}, which is a surprisingly high value in the absence of nucleotide (Table IV). We directly measured the off-rate constants by chasing stopped-flow experiments in which pyrene-acto-mX-S1 was mixed with excess unlabeled actin (Fig. 4*D*). The fitted k_{obs} values of the recorded single exponential transients showed that mX-S1 indeed dissociates unusually rapidly from pyrene-actin in the absence of nucleotide (k_A = 0.41 ± 0.10 s^{-1}), and the off-rate constant is not significantly influenced by the presence of ADP (k_{DA} = 0.34 ± 0.03 s^{-1}; see Table IV). The equilibrium constant of nucleotide-free mX-S1 binding to pyrene-actin calculated from the off- and on-rate constants (K_A = 0.20 μM) was in good agreement with the results of the equilibrium titration experiments of Fig. 4*B* (Table IV). Stopped-flow equilibrium titrations of the type shown in Fig. 4*B, inset*, in the presence of 100 μM ADP yielded a K_{DA} of 1.0 ± 0.2 μM (data not shown), also in reasonable agreement with the ratio of the off- and on-rate constants (Table IV).

ATP-induced Acto-mX-S1 Dissociation, ATP Hydrolysis, and the Weak Actin-binding Interaction—The ATP-induced dissociation of mX-S1 from pyrene-actin was followed by monitoring both pyrene fluorescence and light scattering. The changes in the two signals had opposite signs (pyrene fluorescence increased and light scattering decreased upon pyrene-acto-mX-S1 dissociation) and showed nearly identical dependence of the single exponential k_{obs} values on ATP concentration (Fig. 5*A*). This behavior shows that the dissociation of mX-S1 from pyrene-actin immediately follows the transition from a strongly to a weakly actin-bound state ($k_T + k_{-T} > k_2'$ in Scheme 3). Similarly to other myosins, k_{obs} showed saturation at a high value (k_2' >600 s^{-1}), indicating that ATP binding to acto-mX-S1 is a two-step process (K_1' and k_2'; Scheme 3 and Table IV). The apparent second-order ATP-binding rate constant (k_2'/K_1') was markedly reduced with increasing ionic strength (0.55 ± 0.04 μM^{-1} s^{-1} at I = 125 mM as opposed to 1.8 ± 0.2 μM^{-1} s^{-1} at I = 35 mM; Fig. 5*A* and Table IV).

We performed multiple turnover quenched-flow experiments to assess the transient kinetics of the hydrolysis of ATP after it binds to acto-mX-S1. The observed time courses of P_i production on mixing acto-mX-S1 with excess ATP comprised a single exponential burst with a linear steady-state phase (Fig. 5*B*). The k_{obs} of the burst phase was similar to that of the corresponding pyrene fluorescence and light scattering records both at 10 and 50 μM ATP (Fig. 5*B*). This shows that the ATP-binding process is rate-limiting at these concentrations, consistently with the fast actin-detached ATP hydrolysis rate constant ($k_3 + k_{-3}$ > 80 s^{-1}; *cf.* Fig. 1*B* and Table IV). The amplitude of the burst (0.25 mol of P_i/mol of mX-S1) was similar to that in the quenched-flow experiments performed in the absence of actin (Fig. 1, *B* and *C*).

We assessed the fractional binding of mX-S1 to actin during steady-state ATP hydrolysis by SDS-PAGE analysis following sedimentation of actin-bound mX-S1 by ultracentrifugation (Fig. 5*C*). mX-S1 showed notably high steady-state actin attachment even at moderate actin concentrations and in the absence of any ADP "background" (50% attachment was attained at around 8 and 13 μM actin at ionic strengths of 45 and 125 mM, respectively, see Fig. 5*C*). Inclusion of ADP in the steady-state mixture (at an ATP:ADP ratio of 10:1) caused a further increase in actin attachment (Fig. 5*C*). As expected from the transient kinetics of mX-S1·ADP binding to actin (K_{DA} = 1–2 μM; see Fig. 4*C* and Table IV), practically all mX-S1 was bound to actin even at low actin concentrations in the presence of 200 μM ADP when ATP was not present (Fig. 5*C*).

Actin Activation of Phosphate Release—We investigated the kinetics of P_i release from acto-mX-S1 by double-mixing single turnover stopped-flow experiments in which mX-S1 was first

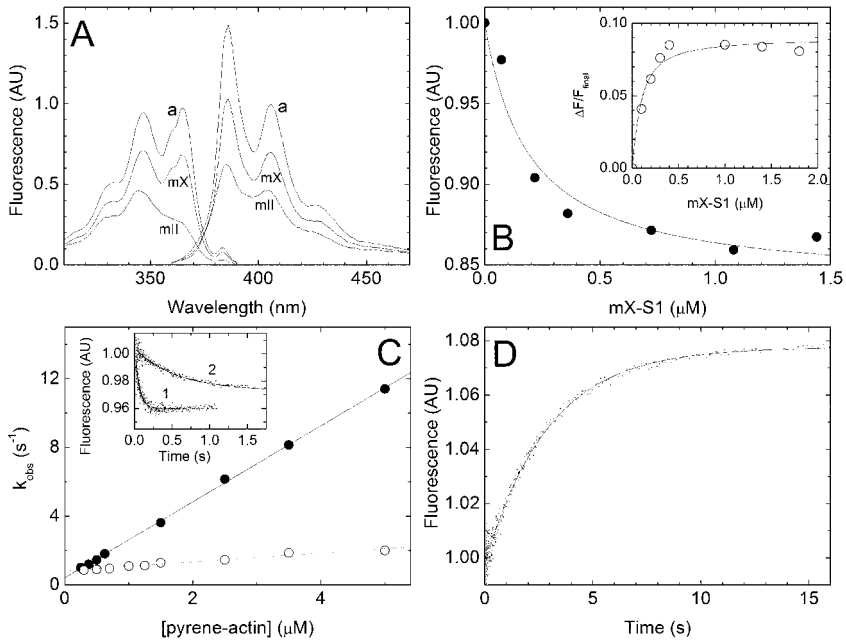

FIG. 4. **Strong binding actin interaction of mX-S1.** *A*, excitation and emission spectra of 1 μM pyrene-actin alone (*a*) and in the presence of 2 μM mX-S1 (*mX*) or 2 μM skeletal muscle myosin II S1 (*mII*). Excitation wavelength was 344 nm for the emission spectra, whereas the excitation spectra were recorded at an emission wavelength of 406 nm. Bandwidths were 1 and 5 nm for the excitation and emission sides, respectively. Data were normalized to the 344 nm excitation and 406 nm emission peaks of pyrene-actin alone. *B*, pyrene fluorescence titration of 30 nM pyrene-actin with increasing concentrations of mX-S1. Excitation was at 344 nm (1 nm bandwidth), and emission was detected at 406 nm (5 nm bandwidth). Data were normalized to the fluorescence intensity of pyrene-actin alone. A hyperbolic fit to the data set yielded a K_A of 0.19 ± 0.03 μM with a final fluorescence level of 0.84 ± 0.02. The *inset* shows the results of a stopped-flow titration where 50 nM pyrene-actin was preincubated with the indicated mX-S1 concentrations and then rapidly mixed with 10 μM ATP to fully dissociate acto-S1 (pre-mixing concentrations indicated). The [mX-S1] dependence of the relative amplitudes (expressed as $\Delta F/F_{final}$) of the recorded single exponential pyrene fluorescence transients (k_{obs} = 4.3 ± 0.5 s^{-1}) was fitted to a quadratic binding equation to yield a K_A of 0.09 ± 0.04 μM and a maximal $\Delta F/F_{final}$ value of 0.09 ± 0.005. *C*, observed rate constants (k_{obs}) of pyrene fluorescence decrease transients recorded on mixing 0.1–0.3 μM mX-S1 with various concentrations of pyrene-actin in the absence (*solid symbols*) and presence (*open symbols*) of 1 mM ADP (in all syringes). Linear fits to the data sets yielded slopes of 2.2 ± 0.02 $\mu M^{-1}s^{-1}$ (k_{-A}) and 0.26 ± 0.02 $\mu M^{-1}s^{-1}$ (k_{-DA}) for mX-S1 and mX-S1·ADP binding to pyrene-actin, respectively. The *y* intercepts indicating the dissociation rate constant from pyrene-actin were 0.41 ± 0.06 s^{-1} (k_A) and 0.81 ± 0.04 s^{-1} (k_{DA}) for mX-S1 and mX-S1·ADP, respectively. The *inset* shows traces of 0.3 μM mX-S1 binding to 5 μM pyrene-actin in the absence (*trace 1*, k_{obs} = 11 s^{-1}) and presence of 1 mM ADP (*trace 2*, k_{obs} = 2.0 s^{-1}). *D*, pyrene fluorescence transient recorded on rapid mixing of a pre-mixture of 0.2 μM pyrene-actin and 0.3 μM mX-S1 with 10 μM unlabeled actin in the absence of nucleotide. A single exponential fit of the transient gave a k_{obs} of 0.36 s^{-1} for mX-S1 dissociation from pyrene-actin (k_A) in the experiment shown. Conditions were as in Fig. 1. Data points shown in *B* and *C* are averages of three experiments.

$$\begin{array}{ccc} & K_D & \\ \mathrm{M} & \leftrightarrow & \mathrm{MD} \\ K_A \downarrow\uparrow & & \downarrow\uparrow K_{DA} \\ \mathrm{AM} & \leftrightarrow & \mathrm{AMD} \\ & K_{AD} & \end{array}$$

SCHEME 2. **Abbreviations used are as follows: *A*, actin; *M*, myosin; *D*, ADP.**

mixed with substoichiometric amounts of ATP (typically, 2 μM mX-S1 and 1 μM ATP were present after the first mix), was incubated for 1–3 s for ATP binding and hydrolysis to occur, and was then mixed with a range of actin concentrations. P_i release was monitored using a fluorescently labeled phosphate-binding protein (MDCC-PBP) (15) present at a concentration of 4 μM in all syringes in all experiments. The ionic strength was reduced to 45 mM in these experiments to obtain measurable (*i.e.* relatively higher) affinities of the weak binding mX-S1 states to actin (K_T and K_{DP} in Scheme 3). The transients recorded after the second rapid mix were single exponential at low actin concentrations, but at higher [actin] two separate phases were observed (Fig. 6*A*). The k_{obs} of the slow phase saturated around 1 s^{-1}, whereas the fast phase k_{obs} increased with increasing actin concentration to >20 s^{-1} at 50 μM actin, showing signs of saturation (Fig. 6*A*). Similarly to the work of White *et al.* (28) on skeletal muscle myosin II S1, we interpret this biphasic behavior as a result of the following processes. After the first mix, an equilibrium mixture of the pre- and post-hydrolysis MT and MDP states forms (Scheme 1). Upon mixing with actin, the fast phase of the MDCC-PBP fluorescence transients arises from actin binding of MDP (K_{DP}; see Scheme 3) followed by the release of P_i from the AMDP quaternary complex (k_4'). The k_{obs} of this phase will be defined as k_4' [actin]/(K_{DP} + [actin]). The slow phase splits off at higher actin concentrations as a result of the presence of an alternative pathway in which actin-attached ATP hydrolysis (k_3' + k_{-3}' ≈1 s^{-1}; see Scheme 3) limits the rate of the oncoming phosphate release and thus determines the k_{obs} of the slow phase of the transients. The fractional amplitudes of the fast and slow phases (~30% fast phase, Fig. 6*B, inset*) remained more or less constant throughout the examined actin concentration range and are in line with the actin-detached ATP hydrolysis equilibrium constant (K_3 = 0.3 ± 0.1; see Table I). Lowering the ATP concentration to 0.5 μM after the first mix did not affect the k_{obs} values and fractional amplitudes (data not shown), demonstrating that the slow phase is not a result of binding of a second ATP molecule to mX-S1 because of an accidental molar excess of ATP over mX-S1 (*e.g.* because of a possible error in protein concentration).

Phosphate release experiments at 125 mM ionic strength, similar to the ones described above, yielded single exponential MDCC-PBP fluorescence transients whose k_{obs} increased slowly with increasing actin concentration to a small value of 1.3 s^{-1} at 33 μM actin (Fig. 6*C*). We surmise that at this higher ionic strength both MT and MDP (Scheme 3) have very low actin affinities, and thus the two phases of P_i release do not separate.

TABLE III
Fluorescent properties of pyrene-acto-S1 complexes
The conditions used are as follows: 25 °C, 20 mM MOPS (pH 7.0), 5 mM $MgCl_2$, 100 mM KCl, 0.1 mM EGTA. Means ± S.D. for $n = 3$ are reported.

	Pyrene-actin	Pyrene-acto-myosin X S1	Pyrene-acto-skeletal muscle myosin II S1	Pyrene-acto-non-muscle myosin IIB S1
Relative fluorescence intensity (excitation at 365 nm)	1.00	0.68 ± 0.05	0.26 ± 0.04	0.25 ± 0.04
Fluorescence anisotropy	0.26 ± 0.02	0.24 ± 0.02	0.20 ± 0.02	0.20 ± 0.02
Stern-Volmer quenching constant (acrylamide) (M^{-1})	5.4 ± 0.2	2.0 ± 0.3	0.5 ± 0.2	1.2 ± 0.2

TABLE IV
Transient kinetic parameters of acto-mX-S1
The conditions used are as follows: 25 °C, 20 mM MOPS (pH 7.0), 5 mM $MgCl_2$, 100 mM KCl, 0.1 mM EGTA ($I = 125$ mM) if not otherwise indicated. Means ± S.D. for $n = 3$ are reported. Numbering of steps refers to Scheme 3.

k_2'/K_1' (μM^{-1} s^{-1}) (pyrene-actin)	0.55 ± 0.04
k_2'/K_1' ($\mu M^{-1}s^{-1}$) ($I = 35$ mM; pyrene-actin, light scattering)	1.8 ± 0.2
K_1' (μM) ($I = 35$ mM; pyrene-actin, light scattering)	260 ± 30
k_2' (s^{-1}) ($I = 35$ mM; pyrene-actin, light scattering)	630 ± 50
K_T (μM) ($I = 45$ mM; numerical analysis)	~40
K_{DP} (μM) ($I = 45$ mM; MDCC-PBP)	130 ± 50
K_{DP} (μM) (MDCC-PBP)	>100
K_3' ($I = 43$ mM; calculated as K_3K_T/K_{DP})	~0.1
$k_3' + k_{-3}'$ (s^{-1}) ($I = 45$ mM; MDCC-PBP)	0.88 ± 0.11
k_4' (s^{-1}) ($I = 45$ mM; MDCC-PBP)	90 ± 30
k_4'/K_{DP} (μM^{-1} s^{-1}) ($I = 45$ mM; MDCC-PBP)	0.56 ± 0.03
k_4'/K_{DP} (μM^{-1} s^{-1}) (MDCC-PBP)	0.019 ± 0.002
k_{AD} (s^{-1}) (pyrene-actin; ADP chasing with mant-ATP)	18 ± 1
k_{-AD} (μM^{-1} s^{-1}) (numerical analysis)	2.1
K_{AD} (μM) (calculated as k_{AD}/k_{-AD})	8.4
k_{-A} (μM^{-1} s^{-1}) (pyrene-actin)	2.1 ± 0.2
k_A (s^{-1}) (pyrene-actin)	0.41 ± 0.10
K_A (μM) (calculated as k_A/k_{-A})	0.20
K_A (μM) (pyrene-actin titrations)	0.14 ± 0.05
k_{-DA} (μM^{-1} s^{-1}) (pyrene-actin)	0.26 ± 0.02
k_{DA} (s^{-1}) (pyrene-actin)	0.34 ± 0.03
K_{DA} (μM) (calculated as k_{DA}/k_{-DA})	1.3
K_{DA} (μM) (pyrene-actin titrations)	1.0 ± 0.3
K_{DA}/K_D	6.2
K_{DA}/K_A	6.8

In a multiple turnover, single-mixing stopped-flow experiment in which 20 μM actin and 1 μM mX-S1 was mixed with 50 μM ATP at $I = 125$ mM, a linear P_i release time profile was observed with no exponential burst phase (data not shown). This behavior indicates that the net rate of P_i release (influenced by all of the parameters $k_3' + k_{-3}'$, K_3, K_T, K_{DP}, and k_4', see Scheme 3) is rate-limiting in the steady-state ATPase cycle in these conditions, in line with the results of the double-mixing experiments discussed above.

ADP Interaction of Acto-mX-S1—ADP binding to and release from pyrene-acto-mX-S1 did not result in a change in pyrene fluorescence, similarly to other myosins (data not shown). Therefore, we monitored the ADP interaction kinetics of acto-mX-S1 by utilizing the inhibitory effect of ADP on the ATP-induced dissociation of the pyrene-acto-mX-S1 complex. In a set of experiments shown in the *main panel* of Fig. 7*A*, pre-mixtures of 0.2 μM pyrene-actin, 0.25 μM mX-S1, and various ADP concentrations were rapidly mixed with 300 μM ATP in the stopped-flow apparatus (pre-mixing concentrations stated), and the resulting dissociation of mX-S1 from pyrene-actin was monitored by recording pyrene fluorescence increase transients. As a function of [ADP] in the pre-mixture, the fitted single exponential k_{obs} values of the transients rapidly decreased from 96 s^{-1} in the absence of ADP to about 20 s^{-1} at 1 μM ADP, and k_{obs} further converged to zero with increasing ADP concentration (Fig. 7*A*). The reduction of k_{obs} with increasing [ADP] can be deduced from two main causes. First, the rate constant of ADP dissociation from acto-mX-S1·ADP may be lower than that of the ATP-induced dissociation of pyrene-acto-mX-S1 at the ATP concentration used ($k_{AD} < 96$ s^{-1}), and thus limit the rate of the reaction as the acto-mX-S1·ADP ternary complex becomes predominant at high [ADP] in the pre-mixture (Scheme 4 depicts the kinetic steps involved in this process). Second, with increasing [ADP], the transient rebinding of ADP instead of ATP to pyrene-acto-mX-S1 may inhibit the ATP-induced acto-S1 dissociation reaction (even if $k_{AD} > 96$ s^{-1}). Theoretically, if the ADP release from acto-S1 is slower than ATP binding, then double exponential transients are to be expected with the fast phase arising from acto-S1 dissociation caused by ATP binding to ADP-free acto-S1 ($[ATP]k_2'/K_1' = 96$ s^{-1}), and the slow phase representing acto-S1 dissociation through the AMD → AM → AMT pathway where the first ADP dissociation step (k_{AD}) is rate-limiting (Scheme 4). The two phases, however, may not be resolvable because of the relatively low experimental signal-to-noise ratio due to the small pyrene fluorescence change (see Fig. 4 and the trace shown in Fig. 7*B, inset*). Therefore, further experiments were necessary to obtain the ADP dissociation and association rate constants (k_{AD} and k_{-AD}). The *inset* of Fig. 7*A* shows the k_{obs} values of single exponential fits to the pyrene fluorescence transients recorded on rapidly mixing 0.15 μM pyrene-actin plus 0.2 μM mX-S1 with a nucleotide mixture consisting of 200 μM ATP plus the indicated ADP concentrations (pre-mixing concentrations indicated). As discussed in a recent detailed investigation of the ADP interaction of pyrene-actomyosin VI (29), double exponential transients would be expected in this reaction, but the two phases were not resolved in our experiments. Nevertheless, the initial (zero [ADP]) k_{obs} decreased to half at 30 μM ADP (Fig. 7*A, inset*).

The k_{obs} of pyrene-acto-mX-S1 dissociation will equal the ADP release rate constant (k_{AD}) if an ADP-saturated pre-mixture ([AMD] ≫ [AM]; see Scheme 4) is rapidly mixed with such a large excess of ATP that ADP rebinding after the mix will not contribute to the transient (*i.e.* $[ATP]\ k_2'/K_1' \gg [ADP]k_{-AD}$). To achieve such conditions, we rapidly mixed a pre-mixture of 0.15 μM pyrene-actin, 0.2 μM mX-S1, and a relatively high concentration of ADP (50 μM, pre-mixing concentrations stated) with increasing ATP concentrations, and we recorded the resulting pyrene fluorescence transients (Fig. 7*B*). A hyperbolic fit to the k_{obs} *versus* [ATP] plot yielded a maximum of 17.6 s^{-1} as the rate constant of ADP release from pyrene-acto-mX-S1 (k_{AD}; see Fig. 7*B*). We used this rate constant together with the rate constants of ATP-induced acto-mX-S1 dissociation (k_2'/K_1'; see Table I) in computational simulations of a kinetic model according to Scheme 4 while leaving the yet unknown ADP-binding rate constant (k_{-AD}) free to float in order to obtain the best global fit of the resulting simulated pyrene fluorescence transients to the experimental traces of Fig. 7, *A* and *B*. The best fit was achieved at $k_{-AD} = 2.1$ μM^{-1} s^{-1}. Force-fitting of single exponentials to the noise-free simulated traces well reproduced the experimental k_{obs} values (*cf. open* and *solid symbols* in Fig. 7, *A* and *B*). The ratio of k_{AD} to k_{-AD} defines a dissociation constant of ADP binding to acto-mX-S1 (K_{AD}) of 8.3 μM (Table IV). This value is thermodynamically consistent with the other actin and ADP-binding equilibrium constants of mX-S1 (K_{AD}/K_D (= 6.2) must equal K_{DA}/K_A (= 6.8) for thermodynamic consistency; see Table IV).

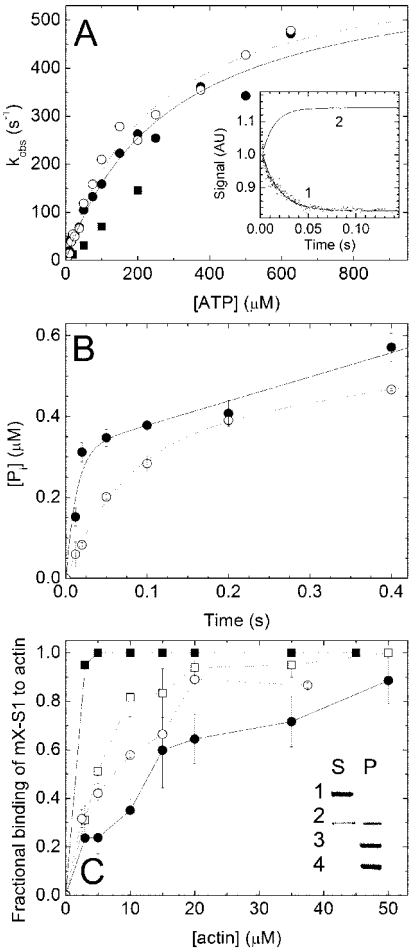

FIG. 5. **ATP-induced dissociation of acto-mX-S1, ATP hydrolysis and weak actin binding.** *A*, observed rate constants (k_{obs}) of ATP-induced pyrene-acto-mX-S1 dissociation on rapid mixing of a premixture of 0.25 μM mX-S1 and 0.15 μM pyrene-actin with the indicated ATP concentrations in the stopped-flow. The recorded transients were fitted to single exponentials. The *solid circles* show k_{obs} values of pyrene fluorescence records (I = 35 mM), and the *open circles* indicate k_{obs} values of light-scattering transients of the same reactions. Hyperbolic fits yielded maximal k_{obs} values of 620 ± 50 and 630 ± 40 s^{-1} (k_2' in Scheme 3) with half-saturation (K_1') at 290 ± 50 and 240 ± 40 μM ATP for pyrene fluorescence and light scattering, respectively. The *solid squares* show pyrene fluorescence k_{obs} values for the same reactions at I = 125 mM. The *inset* shows light scattering (*trace 1*, k_{obs} = 60 s^{-1}) and pyrene fluorescence (*trace 2*, k_{obs} = 66 s^{-1}) traces recorded at 40 μM ATP (I = 35 mM). *B*, time courses of ATP hydrolysis on mixing 1.4 μM mX-S1 and 9 μM actin with 50 μM (*solid symbols*) and 10 μM (*open symbols*) [γ-^{32}P]ATP in the quenched-flow apparatus. Data were fitted to a single exponential burst with a linear steady-state phase. The k_{obs} values of the burst phase were 98 s^{-1} (50 μM ATP) and 14 s^{-1} (10 μM ATP), whereas the burst amplitudes were 0.33 μM (corresponding to 0.24 mol of P_i/mol of mX-S1) in 50 μM ATP and 0.35 μM (0.25 mol P_i/mol mX-S1) in 10 μM ATP. The slope of the linear steady-state phase was fairly uncertain, but its value was in the range expected based on the steady-state ATPase measurements shown in Fig. 3 (0.2–0.5 s^{-1}). *Error bars* in the graph indicate S.D. for n = 4. *C*, actin binding of mX-S1 in the presence of ATP and/or ADP as monitored by acto-mX-S1 cosedimentation. 2 μM mX-S1 was mixed with the indicated actin concentrations and 1 mM ATP (*solid circles, I* = 125 mM; *open circles, I* = 45 mM), a mixture of 1 mM ATP and 100 μM ADP (*open squares, I* = 125 mM), or 200 μM ADP alone (*solid squares, I* = 125 mM). After ultracentrifugation, the amount of mX-S1 heavy chain in the supernatants (*S*) and pellets (*P*) was analyzed by densitometry of SDS-polyacrylamide bands. *Error bars* represent S.D. for n = 2. The *inset* shows mX-S1 heavy chain (2 μM) SDS-polyacrylamide bands of representative samples at I = 125 mM (*S* = supernatant, *P* = pellet). *Row 1*, control in the absence of actin; *row 2*, 20 μM actin and 1 mM ATP; *row 3*, 20 μM actin, 1 mM ATP, and 100 μM ADP; *row 4*, 20 μM actin and 1 mM ADP. To remove potential ADP contamination, 200 units/ml pyruvate kinase and 1 mM phosphoenolpyruvate were added to the samples in which only ATP and no ADP was included. Conditions were as in Fig. 1 except that in *A* and *C* ionic strengths were as indicated.

$$\begin{array}{ccccccccc} & & K_1' & k_2' & & K_3' & & k_4' & K_{AD} \\ \underline{\text{AM}} & \leftrightarrow & \text{AMT} & \rightarrow & \text{AMT} & \leftrightarrow & \text{AMDP} & \rightarrow & \underline{\text{AMD}} \leftrightarrow \underline{\text{AM}} \\ & & & & K_T \downarrow\uparrow & & \downarrow\uparrow K_{DP} & & \\ & & & & \text{MT} & \leftrightarrow & \text{MDP} & & \\ & & & & & K_3 & & & \end{array}$$

SCHEME 3. **Abbreviations used are as follows: *A*, actin; *M*, myosin; *T*, ATP; *D*, ADP; *P*, phosphate.** Strong binding acto-mX-S1 states are *underlined*.

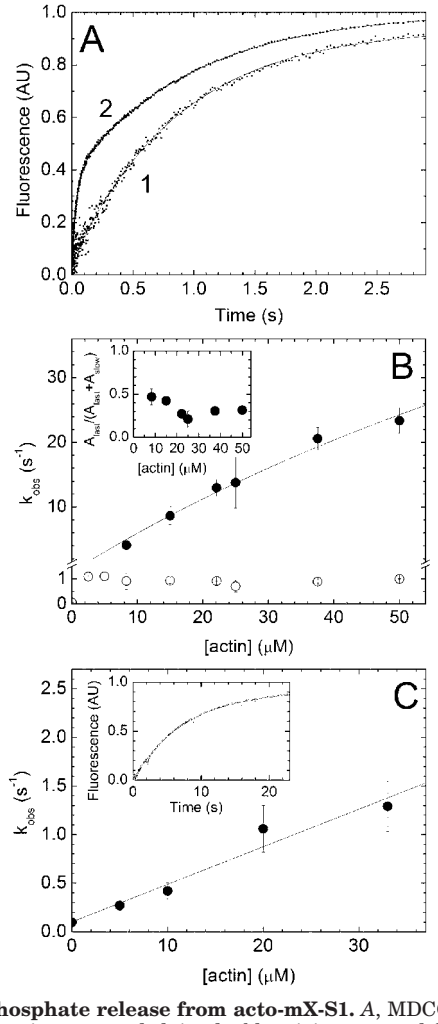

FIG. 6. **Phosphate release from acto-mX-S1.** *A*, MDCC-PBP fluorescence transients recorded in double-mixing stopped-flow experiments at I = 45 mM. 2.3 μM mX-S1 was first mixed with 1.1 μM ATP (concentrations after the first mix), incubated for 1 s for ATP binding and hydrolysis to occur, and then rapidly mixed with increasing concentrations of actin (actin concentrations after the second mix are indicated; data acquisition started at the second mix). At 8 μM actin, a single exponential transient was observed with a k_{obs} of 1.4 s^{-1} (*trace 1*). At 50 μM actin (*trace 2*), the transient was double exponential with k_{obs} values of 25 s^{-1} (35% fractional amplitude) and 1.0 s^{-1} (65%). Traces were normalized to a total amplitude of 1. *B*, dependence of the k_{obs} values of the fast (*solid symbols*) and slow (*open symbols*) phases on actin concentration in P_i release experiments described in *A*. A hyperbolic fit to the fast phase k_{obs} values indicated a maximal k_{obs} (k_4' in Scheme 3) of 90 ± 30 s^{-1} with half-saturation at 130 ± 50 μM actin (K_{DP}). A linear fit to the same data set (not shown) yielded an apparent second-order rate constant of actin binding to the mX-S1·ADP·P_i complex of 0.56 ± 0.03 $\mu M^{-1}s^{-1}$ (k_4'/K_{DP}). *C*, observed rate constants (k_{obs}) of single exponential P_i release transients recorded in double-mixing stopped-flow experiments similar to those of *A* but at I = 125 mM. A linear fit to the dependence of k_{obs} on actin concentration yielded 0.019 ± 0.002 $\mu M^{-1}s^{-1}$ for k_4'/K_{DP}. The y intercept of the fit was 0.03 ± 0.01 s^{-1}, in line with the basal mX-S1 ATPase activity (Table I). The *inset* shows an MDCC-PBP fluorescence trace recorded at 5 μM actin that had a k_{obs} of 0.13 s^{-1}. 4 μM MDCC-PBP was present in all syringes. Conditions were as in Fig. 1, except that ionic strengths were as indicated. *Error bars* indicate S.D. for n = 3.

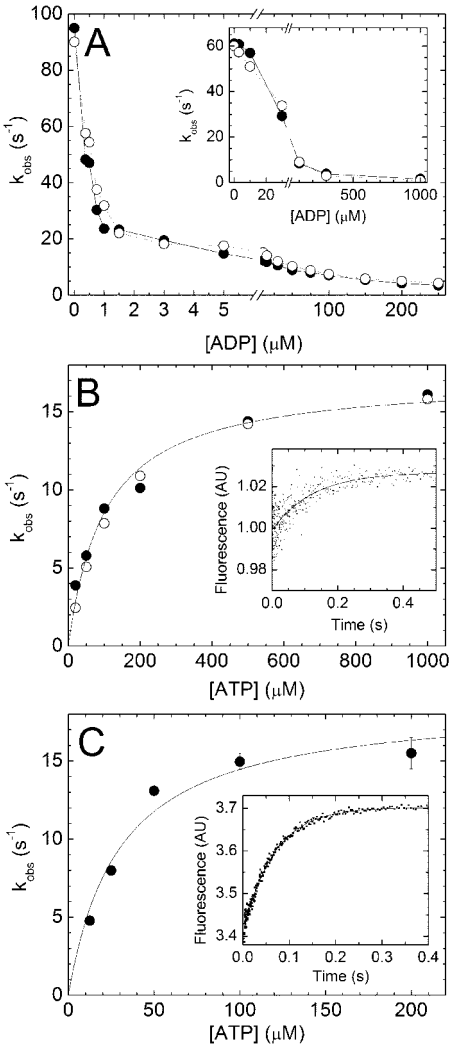

FIG. 7. **ADP kinetics of acto-mX-S1.** *A*, observed rate constants (k_{obs}) of pyrene fluorescence increase transients recorded on mixing a pre-mixture of 0.25 μM mX-S1, 0.2 μM pyrene-actin, and the indicated ADP concentrations with 300 μM ATP in the stopped-flow. The *inset* shows k_{obs} values of pyrene fluorescence transients recorded on rapid mixing of 0.2 μM mX-S1 plus 0.15 μM pyrene-actin with a mixture of 200 μM ATP and the indicated ADP concentrations. Note the breaks in the *x* axes of both panels. *A* and *B*, *solid symbols* show the fitted rate constants of the experimental traces, and *open symbols* indicate the rate constants resulting from kinetic simulations based on the model described in the text. *B*, observed rate constants (k_{obs}) of pyrene fluorescence transients on rapid mixing of a pre-mixture of 0.2 μM mX-S1, 0.15 μM pyrene-actin, and 50 μM ADP with the indicated ATP concentrations in the stopped-flow. A hyperbolic fit to the data set yielded a maximal k_{obs} (= k_{AD}, Schemes 3 and 4) of 17.6 s^{-1}. The *inset* shows a trace obtained at 200 μM ATP that had a k_{obs} of 9.8 s^{-1}. *C*, dependence of the observed rate constants (k_{obs}) of mant-ATP fluorescence transients recorded on rapidly mixing a pre-mixture of 1 μM mX-S1, 12 μM actin, and 30 μM ADP with increasing mant-ATP concentrations in the stopped-flow. Data were fitted to a hyperbola to obtain a maximal k_{obs} (= k_{AD}) of 18.8 s^{-1}. The *inset* shows a transient recorded at 100 μM mant-ATP (k_{obs} = 15 s^{-1}). Conditions were as in Fig. 1. Pre-mixing concentrations are stated throughout this figure. All traces were fitted to single exponentials (see text).

$$\mathrm{AM} + \mathrm{T} \xrightarrow{k_2'/K_1'} \mathrm{A} + \mathrm{MT}$$

$$\mathrm{AM} + \mathrm{D} \overset{K_{AD}}{\leftrightarrow} \mathrm{AMD}$$

SCHEME 4. **Abbreviations used are as follows: *A*, actin; *M*, myosin; *T*, ATP; *D*, ADP.**

We also applied another method for the determination of the k_{DA} rate constant. In these experiments a pre-mixture of 1 μM mX-S1, 12 μM actin, and 30 μM ADP was rapidly mixed with increasing concentrations of mant-ATP in the stopped flow, and the binding of mant-ATP to acto-mX-S1 was monitored by the increase in mant-ATP fluorescence (Fig. 7*C*). Similarly to the experiments of Fig. 7*B*, the ADP dissociation rate constant from acto-mX-S1 (k_{AD}) will limit the k_{obs} of the process at high mant-ATP concentrations (*cf.* Scheme 4). The fitted maximal k_{obs} in these experiments was 18.8 s^{-1} (Fig. 7*C*), in agreement with the results of Fig. 7*B*.

DISCUSSION

Steady-state Distribution of Acto-mX-S1 ATPase Intermediates—We used the determined biochemical parameters to establish a kinetic model of the entire acto-mX-S1 ATPase cycle that can serve as a basis for calculations of functionally important steady-state parameters and predictions of the motile behavior of this myosin. A chief component of the actin activation of the mX-S1 ATPase is a robust (~700-fold) acceleration of phosphate release from the mX-S1·ADP·P_i products complex by actin (k_4 = 0.13 s^{-1}, k_4' ≈90 s^{-1}; see Schemes 1 and 3 and Tables I and IV). However, both the rate constant of P_i release from acto-mX-S1 (k_4') and the ADP release rate constant (k_{AD} = 18 ± 1 s^{-1}) are markedly greater than the maximal steady-state ATPase activity of acto-mX-S1 (4–5 s^{-1}; see Table II). Other steps such as ATP binding to acto-mX-S1, dissociation of acto-mX-S1, or actin-detached ATP hydrolysis are also too fast to act as a single rate-limiting step of the enzymatic cycle. The contributions of multiple processes to steady-state rate limitation can therefore be determined only by global numerical analysis of the enzymatic cycle.

A large majority of the elementary rate constants used in the numerical analysis could be directly extracted from the experimental data. Large uncertainties remain in only two parameters as follows: the equilibrium constant of the actin-attached ATP hydrolysis step (K_3' in Scheme 3), and the actin affinity of the mX-S1·ATP complex (K_T). We could determine both K_3 and K_{DP} with reasonable accuracy, and therefore the values for K_3' and K_T must be interdependent to maintain thermodynamic consistency ($K_3'/K_T = K_3/K_{DP}$). The actin concentration dependences of the steady-state acto-mX-S1 ATPase activity (Fig. 3) and actin attachment ratio (Fig. 5*C*) were used as experimental steady-state data for parameter optimization of K_3' and K_T. (Note that the total actin attachment ratio is the sum of the fractional abundance of all actin-attached steady-state intermediates (AM, AMT, AMDP, and AMD in Scheme 3) and thus it is different from the duty ratio, which is the sum of the fractional abundance of only the strongly actin-bound states (AM and AMD).) Data related to an ionic strength of 45 mm were considered for the analysis because K_{DP} was determined at this ionic strength, and the actin affinity of the weak actin-binding myosin states (K_T and K_{DP}) are generally the parameters having a marked dependence on solution ionic strength. Simulations in which K_T was set to the same value as K_{DP} (=160 μM) and K_3' was thus defined as 0.3 (= K_3 K_T/K_{DP}) yielded a steady-state ATPase activity having a plateau (V_{max}) around 4.5 s^{-1} with a half-saturation at 30 μM actin (K_{ATPase}). These values correspond reasonably well with the experimental data (a V_{max} of 3–5 s^{-1} and a K_{ATPase} of 15–30 μM is expected (Table II)). However, the simulated steady-state actin attachment ratio was much lower than the experimental one (50% attachment was reached at 65 μM actin in the simulation as opposed to the experimental 10–15 μM (Fig. 5*C*)). Therefore, we next lowered K_T 10-fold (to 13 μM), accompanied by a 10-fold reduction in K_3' (to 0.03). These parameters resulted in a steady-state ATPase that rapidly saturated with increasing

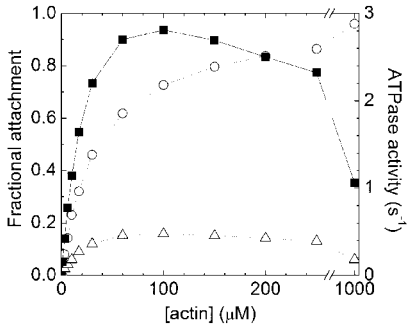

FIG. 8. **Simulated duty ratio, actin attachment, and steady-state acto-mX-S1 ATPase activity.** Results of computational kinetic simulations of the dependence of steady-state properties of mX-S1 on actin concentration are shown. The experimentally determined kinetic constants (Tables I and IV) were fed into a kinetic model of the entire mX-S1/acto-mX-S1 ATPase cycle according to Schemes 1 and 3. Additional parameters used are as follows: K_T = 43 μM (rapid equilibrium); K_{DP} = 130 μM (rapid equilibrium); k_3 = 30 s^{-1}; k_{-3} = 100 s^{-1}; k_3' = 0.1 s^{-1}; k_{-3}' = 1 s^{-1}; k_4' = 90 s^{-1} (irreversible step); [ATP] = 1 mM; and [ADP] = 0. The duty ratio (*i.e.* the sum of the fractional abundance of the strongly actin-bound states (AM and AMD in Scheme 3), shown as *triangles*, left *y* axis) acquired a maximal value of 0.16 at around 100 μM actin. The fractional actin attachment (*i.e.* the sum of the fractional abundance of all (weak and strong) actin-attached states, *circles*, left *y* axis) converged to 1 and showed half-saturation around 25 μM actin. The steady-state ATPase activity (*squares*, *right y* axis) exhibited a maximal value around 3 s^{-1} at 100 μM actin (with half-saturation around 15 μM actin) and then declined to ~1 s^{-1} at high actin concentrations.

actin concentration (K_{ATPase} = 7 μM), but its maximal value (V_{max} = 1.3 s^{-1}) was well below the experimental one. A model with intermediate values, in which K_T was set to 43 μM and K_3' to 0.1, showed reasonably good agreement with the experimental data with regard to all three parameters (the model yielded a V_{max} of 3.5 s^{-1} and a K_{ATPase} of 15 μM, with half-saturation of actin attachment occurring at 25 μM actin, see Fig. 8).

It is remarkable that the actin attachment ratio during steady-state ATP hydrolysis shows half-saturation at an actin concentration (25 μM) that is well below the dissociation constants of both weak actin-binding mX-S1 states (K_T = 43 μM and K_{DP} = 130 μM), and the presence of the strongly actin-bound AMD species (with a fractional occupancy of 10% at 25 μM actin) has only a limited contribution to this phenomenon. At low actin concentrations, the detached MT and MDP states are the predominant steady-state intermediates. With increasing actin concentration, the AMT and, to a more limited extent, the AMD species become the most abundant ones.

The predominance of the AMT complex in the steady-state mixture has two important and somewhat unusual consequences. First, the classically defined duty ratio, which in this case practically equals the fractional occupancy of AMD, will have a maximal value of 16% at around 100 μM actin, but with a further increase in actin concentration it then declines to a value around 6% (Fig. 8). Second, the steady-state ATPase activity will also decline at very high actin concentrations and reach a final value rate-limited by actin-attached ATP hydrolysis ($k_3' + k_{-3}' \approx 1$ s^{-1}, see Fig. 8). Unfortunately, the experimental demonstration of these phenomena is strongly hindered by major technical difficulties because the pyrene-actin signal change on mX-S1 binding (that could be used for duty ratio measurement) is small, and the reduction in the steady-state ATPase activity becomes significant only at actin concentrations well above 200 μM.

Another important feature predicted by the model is that the presence of even high concentrations of ADP will have only a limited effect on the steady-state properties of acto-mX-S1. At 100 μM actin and an ATP concentration of 1 mM, the introduction of an 1 mM ADP background into the steady-state simulation only decreased the acto-mX-S1 ATPase activity by 20% and caused a small increase in the total actin attachment ratio (from 73 to 76%), but the duty ratio was notably elevated (from 16 to 28%).

As an alternative to the above model, it is conceivable that a slow isomerization between two different ADP-bound acto-mX-S1 states (which would occur between steps k_4' and k_{AD} in Scheme 3) could limit the steady-state flux through the ATPase cycle. Such a step would remain undetected in the experiments of Fig. 7 if it was highly favorable in the left-to-right direction in Scheme 3. (In this case, only the "post-step" species would be represented in the acto-mX-S1·ADP pre-mixtures.) However, the strong dependence of the steady-state K_{ATPase} on ionic strength (Table II) and the absence of a rapid burst phase of P_i release in single-mixing stopped-flow experiments indicate that the kinetic partitioning between the weak actin-binding intermediates is a major determinant of the steady-state rate even in this case. Thus, in order to maintain a steady-state V_{max} around 4 s^{-1}, the rate constant of this hypothetical acto-mX-S1·ADP isomerization must be in the same range (or faster) than the k_{AD} value determined in this study (18 s^{-1}).

Taken together, the data show that the main kinetic pattern of myosin X is different from that of the high duty ratio motors myosin V and VI (25, 26); its duty ratio is lower, and the entry into the strong binding AMD state contributes more to steady-state rate limitation than the exit from this state (*i.e.* ADP release). These findings are consistent with the results of Homma *et al.* (9) showing that, unlike myosin V, a heavy mero-myosin-like myosin X construct showed *in vitro* motile activity only at fairly high surface densities, and the presence of ADP had little effect on its ATPase activity. On the other hand, the predicted maximal duty ratio of myosin X (16%) is notably higher than that of skeletal and smooth muscle myosins (4%) (30), in line with the fact that the surface density required for smooth muscle myosin II *in vitro* motility was even higher than in the case of myosin X (9).

Two ADP-bound States of mX-S1—We present kinetic evidence showing that mX-S1 adopts at least two different ADP-bound structural states in the absence of actin (see Scheme 1). Analysis of our transient kinetic data indicates that one of the ADP states (MD) has a tryptophan fluorescence intensity similar to that of nucleotide-free mX-S1, whereas the other state (M*D) exhibits a slightly elevated fluorescence intensity (by about 10%). The two states are in reversible equilibrium (K_5 = 0.37 ± 0.03 at 25 °C and I = 125 mM; see Table I). The existence of multiple ADP-bound states has been demonstrated in the case of several myosin II isoforms (31, 32). However, their rate constant of interconversion in mX-S1 ($k_5 + k_{-5} \approx 4$ s^{-1}) is about 50-fold smaller than those reported for myosin II. Based on the fact that ATP causes an ~3-fold larger increase in tryptophan fluorescence than ADP, we propose that the MD ↔ M*D step (K_5) is different from the transition between the crystallographically identified switch II open-to-closed transition that is coupled to ATP hydrolysis and is accompanied by a large rotation of the neck (lever arm) region (this transition is likely to occur on the M*T ↔ M**DP step (K_3 in Scheme 1) (33)). Myosin X possesses the so-called relay loop tryptophan (Trp-481 in mX-S1) that has been shown to be sensitive to both nucleotide binding and the open-closed transition in various myosin II isoforms (34–38), whereas it lacks tryptophans at the nucleotide-binding pocket that also showed fluorescence changes on nucleotide binding to skeletal muscle myosin II (Trp-113 and Trp-131 in skeletal myosin) (37). Thus, it is likely that the tryptophan fluorescence changes during the mX-S1 ATPase cycle are largely due to Trp-481. It is noteworthy that, uniquely

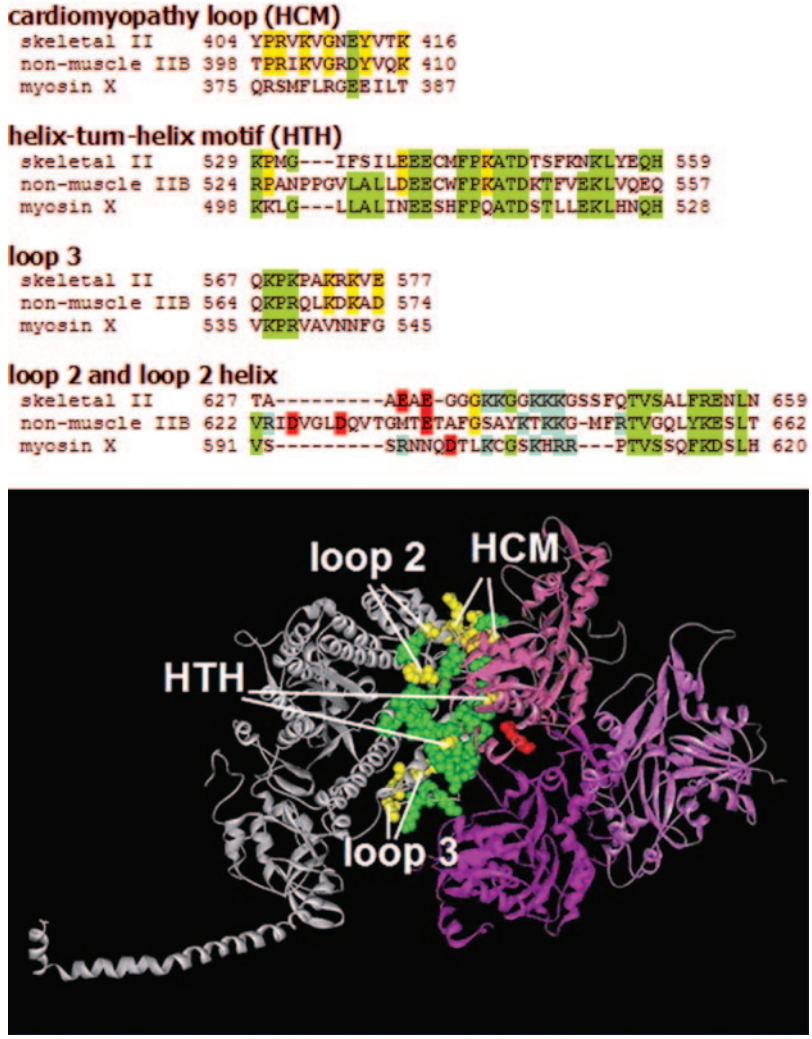

FIG. 9. **Amino acid sequence comparison of the actin binding interface of myosins II and X.** The *upper panel* shows amino acid sequence alignments of rabbit skeletal muscle myosin II, human non-muscle myosin IIB, and bovine myosin X for four major structural elements of the actin-binding interface. Positions that are occupied by residues of similar chemical character in the two myosin II isoforms but by a very different one in myosin X are highlighted in *yellow*. The *green* color marks positions in which myosin X shows identity with at least one of the myosin II isoforms. Loop 2 residues with positively or negatively charged side chains are marked with *blue* and *red*, respectively. The *lower panel* highlights the residues marked *yellow* and *green* in the context of the structural model of the rigor actomyosin II complex (50). The myosin II heavy chain head fragment is colored *gray* (light chains are omitted for clarity). Actin monomers are shown in different shades of *magenta*. The actin residue Arg-372 of the relevant monomer (the closest "visible" one to Cys-374 labeled with the pyrene fluorophore in pyrene-actin) is highlighted in *red*. Figure was prepared using ClustalW (*upper panel*) and WebLabViewerPro 4.0 (*lower panel*).

among myosins, myosin X has another tryptophan residue in the relay loop (Trp-486) that is conserved within this class (the homologous position is occupied by other aromatic residues in myosin II and most other myosins (39)). Another potentially sensitive tryptophan residue in mX-S1 that is missing from myosin II is located at the basis of the lever arm (Trp-717; this tryptophan is present in some myosin I, III, VII, XIII, and XIV isoforms (39)).

The first step of ADP binding to mX-S1 (M ↔ MD transition, see K_6 in Scheme 1) exhibits strikingly similar kinetic parameters to the acto-mX-S1 ADP binding step (K_{AD} in Scheme 3) (on-rates, 2.1–4.3 $\mu M^{-1}s^{-1}$ (k_{-6}) *versus* 2.1 μM^{-1} s^{-1} (k_{-AD}); off-rates, 13–16 s^{-1} (k_6) *versus* 18 s^{-1} (k_{AD}); and equilibrium constants, 3.7–6.3 μM (K_6) *versus* 8.4 μM (K_{AD})). It can thus be inferred that the strong binding interaction of mX-S1 with actin causes little or no change in the structural dynamics of ADP binding into the nucleotide pocket of mX-S1, and the MD state (which is significantly populated in the absence of actin) may be structurally very similar to the acto-mX-S1·ADP ternary complex (AMD state). Actin thus does not accelerate the ADP release step *per se*, but it rather changes the conformational distribution of mX-S1·ADP and favors a lower ADP affinity state (MD) that is present even in the absence of actin. (One may even surmise that the M*D state is off the main pathway of the basal mX-S1 ATPase cycle and represents only a side branch. Such an alteration in the mechanism would not change the ATP-related kinetic behavior of the enzyme.) The absence of a marked acceleration of the ADP release step by actin is not without precedent in the myosin superfamily; nonmuscle myosin IIA (21), IIB (17), and myosin VI (29, 40) have been shown previously to exhibit a similar behavior.

Spectral and Kinetic Properties of the Pyrene-Acto-mX-S1 Complex—Our pyrene-actin fluorescence studies indicate that the rigor (nucleotide-free) complex of mX-S1 with actin shows several distinctive features. The spectral changes of pyrene-actin on binding to mX-S1 are markedly different from those on interaction with different myosin II isoforms (Fig. 4*A* and Table III); the acto-mX-S1 affinity is remarkably low (K_A = 0.14 ± 0.05 μM; see Fig. 4*B* and Table IV), and the off-rate constant of mX-S1 from pyrene-actin is fast (k_A = 0.41 ± 0.10 s^{-1}; see Fig. 4*D*). Most myosin isoforms investigated to date, including smooth muscle myosin II (20), vertebrate non-muscle myosin II (17, 21), *Dictyostelium* myosin II (22), as well as myosins I (23, 24), V (25), and VI (26), show rigor dissociation constants in the nanomolar range, and the dissociation rate constants fall usually below 0.01 s^{-1} under similar temperature and ionic strength conditions to those in the current study. An intriguing exception is skeletal muscle myosin, which showed a very similar profile to mX-S1 (K_A = 0.11 μM, k_A = 0.22 s^{-1} at 20 °C, I = 125 mM) in the pyrene fluorescence study of Criddle *et al.* (18). Despite a number of recently published studies (41–44), views about the atomic structure of the rigor actomyosin complex are still controversial even in the case of the best studied myosin II class. To assess the structural basis of the unusual fluorescent and kinetic properties of pyrene-acto-mX-S1, we made amino acid sequence comparisons of the major structural elements of

the actin-binding interface of myosins II and X (Fig. 9). The helix-turn-helix motif of the strong actin-binding interface is the myosin structural element that directly interacts with the actin segment that contains the Cys-374 residue carrying the pyrene fluorophore. Most interestingly, this region of myosin is fairly conserved between classes II and X (Fig. 9). The major differences between the primary structure of the actin interface of myosins II and X locate to regions more distant from the pyrene fluorophore attachment site, primarily to the so-called cardiomyopathy loop and, to a lesser extent, to loop 3. It is thus not possible to simply relate the spectral differences of pyrene-acto-S1 complexes to differences in the sequence of a limited set of amino acid position(s) that directly interact with the fluorophore. The spectral and kinetic differences possibly result from differences in the large scale structural dynamics of the actomyosin interface. We could not identify acto-mX-S1 conformational substrates in our steady-state fluorescence measurements. Future time-resolved fluorescence studies will likely yield insights into these properties, and the distinctive features of myosin X may also contribute to our general view of the actomyosin interaction.

Role of the Biochemical Properties of mX-S1 in Cellular Functions—Myosins exert their motile activity during cyclic interaction with actin. As emphasized in a recent review (8) on the biochemical adaptations of myosins to different cellular environments, a supramolecular ensemble of any myosin must be able to maintain continuous attachment to actin during a contractile event that may span a large number of enzymatic cycles and corresponding mechanical steps. Each myosin isoform must therefore be processive *as a functional unit* to be capable of motile activity. A unique feature of myosin X within the myosin superfamily is that among its various effector domains in the tail region it has PH3 domains that bind to membrane phospholipids. Therefore, this myosin probably exerts its cellular functions in a markedly different supramolecular organization from that of many other actin-based motors, *e.g.* the thick filaments of myosin II or the single molecule motility of myosin V. The predicted maximal duty ratio of myosin X is 16% (in the absence of background ADP), which implies that myosin X would not be able to perform myosin V-like double-headed single molecule stepping, for which a strong (stereospecific) attachment of at least one of the heads to actin at any time and therefore a single-head duty ratio of at least 50% is a prerequisite. Regardless of this, the full-length myosin X molecule is predicted to be double-headed based on the presence of a putative coiled-coil region in the tail domain. However, based on recent doubts about the dimeric nature of myosin VI, one must use caution regarding such predictions based on amino acid sequence (45). Although the dimerization of heavy chains is probably of functional significance, the membrane-attached nature of myosin X is likely to be the main determinant of the functional constraints imposed on this motor. A small array of membrane-bound myosin X molecules (consisting of at least 8–10 heads) with a duty ratio of 0.16 may already be capable of processive movement. Furthermore, it is reasonable that there would be no strong demand for a high duty ratio in a tight spatial arrangement of the actin cytoskeleton and the plasma membrane (especially in filopodia), because such an arrangement can effectively prevent the diffusion of myosin X away from the actin filament. Correspondingly, a recent elegant study (46) has demonstrated the importance of PH domain-mediated membrane attachment in motor function and processivity of the KIF1A kinesin isoform.

It is an intriguing possibility that myosin X may be capable of diffusive sliding along actin in the weakly actin-attached states that are the most abundant steady-state intermediates, while cyclic power strokes carried out in a strongly (stereospecifically) actin-bound state could ensure a net directionality of the movement toward the barbed end of the actin filament. Such a behavior may be related to the interesting "back-and-forth" patterns of intrafilopodial motility of myosin X-containing puncta *in vivo* (4). It may also be of interest to determine whether the weak actin-binding states of myosin X are in rapid equilibrium with actin as they are in the case of myosin II, or the rate of actin detachment of these states is also a significant determinant of the motile properties. It should also be noted that the biochemical properties and low calculated duty ratio of the single-headed mX-S1 construct presented in the current work do not provide a simple explanation to the fact that a heavy meromyosin-like (double-headed) myosin X construct appears to be able to actively move out to filopodial tips, presumably as a single molecule in the absence of a tail that could provide membrane attachment (4). It is possible that in double-headed myosin X, a strain-sensitive head-head coordination mechanism influences the rate constants of nucleotide binding and/or dissociation, thereby increasing processivity. Such effects have been demonstrated in the case of myosins V and VI (29, 47, 48).

Although myosin X actively moves out to the tips of filopodia (and so does myosin XVa to stereocilial tips), other motors such as myosin V do not show this behavior (4, 49). A biochemical explanation for this difference could be that the actin interaction of myosin X (and possibly XVa) is regulated by a specific set of actin-associated proteins (*e.g.* various isoforms of tropomyosin) that do not have a similar effect on the motility of other motors such as myosin V. A series of important questions regarding the function and mechanism of myosin X remain to be addressed in future cell biological and biochemical/biophysical studies.

Acknowledgments—We thank Dr. David Corey (Harvard Medical School) for the bovine myosin X cDNA clone; Lingfeng Chen for engineering the DNA construct for mX-S1; Dr. Howard White (Eastern Virginia Medical School) for the gift of MDCC-PBP; Estelle V. Harvey, Yue Zhang, and Antoine F. Smith for expert technical assistance; and Judit Tóth for discussions.

REFERENCES

1. Berg, J. S., Derfler, B. H., Pennisi, C. M., Corey, D. P., and Cheney, R. E. (2000) *J. Cell Sci.* **113,** 3439–3451
2. Berg, J. S., Powell, B. C., and Cheney, R. E. (2001) *Mol. Biol. Cell* **12,** 780–794
3. Mashanov, G. I., Tacon, D., Peckham, M., and Molloy, J. E. (2004) *J. Biol. Chem.* **279,** 15274–15280
4. Berg, J. S., and Cheney, R. E. (2002) *Nat. Cell Biol.* **4,** 246–250
5. Tokuo, H., and Ikebe, M. (2004) *Biochem. Biophys. Res. Commun.* **319,** 214–220
6. Cox, D., Berg, J. S., Cammer, M., Chinegwundoh, J. O., Dale, B. M., Cheney, R. E., and Greenberg, S. (2002) *Nat. Cell Biol.* **4,** 469–477
7. Zhang, H., Berg, J. S., Li, Z., Wang, Y., Lang, P., Sousa, A. D., Bhaskar, A., Cheney, R. E., and Stromblad, S. (2004) *Nat. Cell Biol.* **6,** 523–531
8. De La Cruz, E. M., and Ostap, E. M. (2004) *Curr. Opin. Cell Biol.* **16,** 61–67
9. Homma, K., Saito, J., Ikebe, R., and Ikebe, M. (2001) *J. Biol. Chem.* **276,** 34348–34354
10. Wang, F., Harvey, E. V., Conti, M. A., Wei, D., and Sellers, J. R. (2000) *Biochemistry* **39,** 5555–5560
11. Margossian, S. S., and Lowey, S. (1982) *Methods Enzymol.* **85,** 55–71
12. Okamoto, Y., and Sekine, T. (1985) *J. Biochem.* (*Tokyo*) **98,** 1143–1145
13. Spudich, J. A., and Watt, S. (1971) *J. Biol. Chem.* **246,** 4866–4871
14. Cooper, J. A., Walker, S. B., and Pollard, T. D. (1983) *J. Muscle Res. Cell Motil.* **4,** 253–262
15. Brune, M., Hunter, J. L., Corrie, J. E., and Webb, M. R. (1994) *Biochemistry* **33,** 8262–8271
16. Trentham, D. R., Bardsley, R. G., Eccleston, J. F., and Weeds, A. G. (1972) *Biochem. J.* **126,** 635–644
17. Wang, F., Kovacs, M., Hu, A., Limouze, J., Harvey, E. V., and Sellers, J. R. (2003) *J. Biol. Chem.* **278,** 27439–27448
18. Criddle, A. H., Geeves, M. A., and Jeffries, T. (1985) *Biochem. J.* **232,** 343–349
19. Kouyama, T., and Mihashi, K. (1981) *Eur. J. Biochem.* **114,** 33–38
20. Cremo, C. R., and Geeves, M. A. (1998) *Biochemistry* **37,** 1969–1978
21. Kovacs, M., Wang, F., Hu, A., Zhang, Y., and Sellers, J. R. (2003) *J. Biol. Chem.* **278,** 38132–38140
22. Furch, M., Fujita-Becker, S., Geeves, M. A., Holmes, K. C., and Manstein, D. J. (1999) *J. Mol. Biol.* **290,** 797–809
23. Coluccio, L. M., and Geeves, M. A. (1999) *J. Biol. Chem.* **274,** 21575–21580
24. El Mezgueldi, M., Tang, N., Rosenfeld, S. S., and Ostap, E. M. (2002) *J. Biol. Chem.* **277,** 21514–21521

25. de la Cruz, E. M., Wells, A. L., Rosenfeld, S. S., Ostap, E. M., and Sweeney, H. L. (1999) *Proc. Natl. Acad. Sci. U. S. A.* **96,** 13726–13731
26. de la Cruz, E. M., Ostap, E. M., and Sweeney, H. L. (2001) *J. Biol. Chem.* **276,** 32373–32381
27. Malnasi-Csizmadia, A., Pearson, D. S., Kovacs, M., Woolley, R. J., Geeves, M. A., and Bagshaw, C. R. (2001) *Biochemistry* **40,** 12727–12737
28. White, H. D., Belknap, B., and Webb, M. R. (1997) *Biochemistry* **36,** 11828–11836
29. Robblee, J. P., Olivares, A. O., and de la Cruz, E. M. (2004) *J. Biol. Chem.* **279,** 38608–38617
30. Harris, D. E., and Warshaw, D. M. (1993) *J. Biol. Chem.* **268,** 14764–14768
31. Trybus, K. M., and Taylor, E. W. (1982) *Biochemistry* **21,** 1284–1294
32. Kovacs, M., Malnasi-Csizmadia, A., Woolley, R. J., and Bagshaw, C. R. (2002) *J. Biol. Chem.* **277,** 28459–28467
33. Geeves, M. A., and Holmes, K. C. (1999) *Annu. Rev. Biochem.* **68,** 687–728
34. Batra, R., and Manstein, D. J. (1999) *Biol. Chem.* **380,** 1017–1023
35. Malnasi-Csizmadia, A., Woolley, R. J., and Bagshaw, C. R. (2000) *Biochemistry* **39,** 16135–16146
36. Malnasi-Csizmadia, A., Kovacs, M., Woolley, R. J., Botchway, S. W., and Bagshaw, C. R. (2001) *J. Biol. Chem.* **276,** 19483–19490
37. Park, S., and Burghardt, T. P. (2000) *Biochemistry* **39,** 11732–11741
38. Yengo, C. M., Chrin, L. R., Rovner, A. S., and Berger, C. L. (2000) *J. Biol. Chem.* **275,** 25481–25487
39. Sellers, J. R. (1999) *Myosins*, 2nd Ed., Oxford University Press, New York
40. Sato, O., White, H. D., Inoue, A., Belknap, B., Ikebe, R., and Ikebe, M. (2004) *J. Biol. Chem.* **279,** 28844–28854
41. Conibear, P. B., Bagshaw, C. R., Fajer, P. G., Kovacs, M., and Malnasi-Csizmadia, A. (2003) *Nat. Struct. Biol.* **10,** 831–835
42. Coureux, P. D., Wells, A. L., Menetrey, J., Yengo, C. M., Morris, C. A., Sweeney, H. L., and Houdusse, A. (2003) *Nature* **425,** 419–423
43. Holmes, K. C., Angert, I., Kull, F. J., Jahn, W., and Schroder, R. R. (2003) *Nature* **425,** 423–427
44. Reubold, T. F., Eschenburg, S., Becker, A., Kull, F. J., and Manstein, D. J. (2003) *Nat. Struct. Biol.* **10,** 826–830
45. Lister, I., Schmitz, S., Walker, M., Trinick, J., Buss, F., Veigel, C., and Kendrick-Jones, J. (2004) *EMBO J.* **23,** 1729–1738
46. Klopfenstein, D. R., and Vale, R. D. (2004) *Mol. Biol. Cell* **15,** 3729–3739
47. Baker, J. E., Krementsova, E. B., Kennedy, G. G., Armstrong, A., Trybus, K. M., and Warshaw, D. M. (2004) *Proc. Natl. Acad. Sci. U. S. A.* **101,** 5542–5546
48. Rosenfeld, S. S., and Sweeney, H. L. (2004) *J. Biol. Chem.* **279,** 40100–40111
49. Belyantseva, I. A., Boger, E. T., and Friedman, T. B. (2003) *Proc. Natl. Acad. Sci. U. S. A.* **100,** 13958–13963
50. Chen, L. F., Winkler, H., Reedy, M. K., Reedy, M. C., and Taylor, K. A. (2002) *J. Struct. Biol.* **138,** 92–104